

Superresolution optical magnetic imaging and spectroscopy using individual electronic spins in diamond

JEAN-CHRISTOPHE JASKULA,^{1,2,3,6} ERIK BAUCH,^{1,3,6} SILVIA ARROYO-CAMEJO,⁴ MIKHAIL D. LUKIN,¹ STEFAN W. HELL,⁴ ALEXEI S. TRIFONOV,^{1,2,3,5} AND RONALD L. WALSWORTH^{1,2,3,*}

¹Department of Physics, Harvard University, Cambridge, Massachusetts 02138, USA

²Harvard-Smithsonian Center for Astrophysics, Cambridge, Massachusetts 02138, USA

³Center for Brain Science, Harvard University, Cambridge, Massachusetts 02138, USA

⁴Department of NanoBiophotonics, Max Planck Society, Am Fassberg 11, 37077 Göttingen, Germany

⁵Ioffe Physical-Technical Institute RAS, Saint Petersburg, Russia

⁶These authors contributed equally to this work

*rwalsworth@cfa.harvard.edu

Abstract: Nitrogen vacancy (NV) color centers in diamond are a leading modality for both superresolution optical imaging and nanoscale magnetic field sensing. In this work, we address the key challenge of performing optical magnetic imaging and spectroscopy selectively on multiple NV centers that are located within a diffraction-limited field-of-view. We use spin-RESOLFT microscopy to enable precision nanoscale mapping of magnetic field patterns with resolution down to ~20 nm, while employing a low power optical depletion beam. Moreover, we use a shallow NV to demonstrate the detection of proton nuclear magnetic resonance (NMR) signals exterior to the diamond, with 50 nm lateral imaging resolution and without degrading the proton NMR linewidth.

© 2017 Optical Society of America

OCIS codes: (180.0180) Microscopy; (100.6640) Superresolution; (020.0020) Atomic and molecular physics; (130.6010) Sensors

References and links

1. M. W. Doherty, N. B. Manson, P. Delaney, F. Jelezko, J. Wrachtrup, and L. C. L. Hollenberg, "The nitrogen-vacancy colour centre in diamond," *Phys. Rep.* **528**(1), 1–45 (2013).
2. L. Rondin, J.-P. Tetienne, S. Rohart, A. Thiaville, T. Hingant, P. Spinicelli, J.-F. Roch, and V. Jacques, "Stray-field imaging of magnetic vortices with a single diamond spin," *Nat. Commun.* **4**, 2279 (2013).
3. T. van der Sar, F. Casola, R. Walsworth, and A. Yacoby, "Nanometre-scale probing of spin waves using single-electron spins," *Nat. Commun.* **6**, 7886 (2015).
4. A. O. Sushkov, I. Lovchinsky, N. Chisholm, R. L. Walsworth, H. Park, and M. D. Lukin, "Magnetic resonance detection of individual proton spins using quantum reporters," *Phys. Rev. Lett.* **113**(19), 197601 (2014).
5. I. Lovchinsky, A. O. Sushkov, E. Urbach, N. P. de Leon, S. Choi, K. De Greve, R. Evans, R. Gertner, E. Bersin, C. Müller, L. McGuinness, F. Jelezko, R. L. Walsworth, H. Park, and M. D. Lukin, "Nuclear magnetic resonance detection and spectroscopy of single proteins using quantum logic," *Science* **351**(6275), 836–841 (2016).
6. J. F. Barry, M. J. Turner, J. M. Schloss, D. R. Glenn, Y. Song, M. D. Lukin, H. Park, and R. L. Walsworth, "Optical magnetic detection of single-neuron action potentials using quantum defects in diamond," *Proc. Natl. Acad. Sci. U.S.A.* **113**(49), 14133–14138 (2016).
7. D. Le Sage, K. Arai, D. R. Glenn, S. J. DeVience, L. M. Pham, L. Rahn-Lee, M. D. Lukin, A. Yacoby, A. Komeili, and R. L. Walsworth, "Optical magnetic imaging of living cells," *Nature* **496**(7446), 486–489 (2013).
8. D. R. Glenn, K. Lee, H. Park, R. Weissleder, A. Yacoby, M. D. Lukin, H. Lee, R. L. Walsworth, and C. B. Connolly, "Single-cell magnetic imaging using a quantum diamond microscope," *Nat. Methods* **12**(8), 736–738 (2015).
9. R. R. Fu, B. P. Weiss, E. A. Lima, R. J. Harrison, X.-N. Bai, S. J. Desch, D. S. Ebel, C. Suavet, H. Wang, D. Glenn, D. Le Sage, T. Kasama, R. L. Walsworth, and A. T. Kuan, "Solar nebula magnetic fields recorded in the Semarkona meteorite," *Science* **346**(6213), 1089–1092 (2014).
10. F. Dolde, I. Jakobi, B. Naydenov, N. Zhao, S. Pezzagna, C. Trautmann, J. Meijer, P. Neumann, F. Jelezko, and J. Wrachtrup, "Room-temperature entanglement between single defect spins in diamond," *Nat. Phys.* **9**(3), 139–143 (2013).

11. J. Cai, A. Retzker, F. Jelezko, and M. B. Plenio, "A large-scale quantum simulator on a diamond surface at room temperature," *Nat. Phys.* **9**(3), 168–173 (2013).
12. G. Balasubramanian, I. Y. Chan, R. Kolesov, M. Al-Hmoud, J. Tisler, C. Shin, C. Kim, A. Wojcik, P. R. Hemmer, A. Krueger, T. Hanke, A. Leitenstorfer, R. Bratschitsch, F. Jelezko, and J. Wrachtrup, "Nanoscale imaging magnetometry with diamond spins under ambient conditions," *Nature* **455**(7213), 648–651 (2008).
13. M. S. Grinolds, M. Warner, K. De Greve, Y. Dovzhenko, L. Thiel, R. L. Walsworth, S. Hong, P. Maletinsky, and A. Yacoby, "Subnanometre resolution in three-dimensional magnetic resonance imaging of individual dark spins," *Nat. Nanotechnol.* **9**(4), 279–284 (2014).
14. K. Arai, C. Belthangady, H. Zhang, N. Bar-Gill, S. J. DeVience, P. Cappellaro, A. Yacoby, and R. L. Walsworth, "Fourier magnetic imaging with nanoscale resolution and compressed sensing speed-up using electronic spins in diamond," *Nat. Nanotechnol.* **10**(10), 859–864 (2015).
15. V. Zablotskii, T. Polyakova, O. Lunov, and A. Dejneka, "How a high-gradient magnetic field could affect cell life," *Sci. Rep.* **6**(1), 37407 (2016).
16. E. H. Chen, O. Gaathon, M. E. Trusheim, and D. Englund, "Wide-field multispectral super-resolution imaging using spin-dependent fluorescence in nanodiamonds," *Nano Lett.* **13**(5), 2073–2077 (2013).
17. M. Pfender, N. Aslam, G. Waldherr, P. Neumann, and J. Wrachtrup, "Single-spin stochastic optical reconstruction microscopy," *Proc. Natl. Acad. Sci. U.S.A.* **111**(41), 14669–14674 (2014).
18. P. C. Maurer, J. R. Maze, P. L. Stanwix, L. Jiang, A. V. Gorshkov, A. A. Zibrov, B. Harke, J. S. Hodges, A. S. Zibrov, A. Yacoby, D. Twitchen, S. W. Hell, R. L. Walsworth, and M. D. Lukin, "Far-field optical imaging and manipulation of individual spins with nanoscale resolution," *Nat. Phys.* **6**(11), 912–918 (2010).
19. D. Wildanger, J. R. Maze, and S. W. Hell, "Diffraction unlimited all-optical recording of electron spin resonances," *Phys. Rev. Lett.* **107**(1), 017601 (2011).
20. S. Arroyo-Camejo, M.-P. Adam, M. Besbes, J.-P. Hugonin, V. Jacques, J.-J. Greffet, J.-F. Roch, S. W. Hell, and F. Treussart, "Stimulated emission depletion microscopy resolves individual nitrogen vacancy centers in diamond nanocrystals," *ACS Nano* **7**(12), 10912–10919 (2013).
21. E. Rittweger, K. Y. Han, S. E. Irvine, C. Eggeling, and S. W. Hell, "STED microscopy reveals crystal colour centres with nanometric resolution," *Nat. Photonics* **3**(3), 144–147 (2009).
22. K. Y. Han, S. K. Kim, C. Eggeling, and S. W. Hell, "Metastable dark States enable ground state depletion microscopy of nitrogen vacancy centers in diamond with diffraction-unlimited resolution," *Nano Lett.* **10**(8), 3199–3203 (2010).
23. J. R. Maze, P. L. Stanwix, J. S. Hodges, S. Hong, J. M. Taylor, P. Cappellaro, L. Jiang, M. V. G. Dutt, E. Togan, A. S. Zibrov, A. Yacoby, R. L. Walsworth, and M. D. Lukin, "Nanoscale magnetic sensing with an individual electronic spin in diamond," *Nature* **455**(7213), 644–647 (2008).
24. S. J. DeVience, L. M. Pham, I. Lovchinsky, A. O. Sushkov, N. Bar-Gill, C. Belthangady, F. Casola, M. Corbett, H. Zhang, M. Lukin, H. Park, A. Yacoby, and R. L. Walsworth, "Nanoscale NMR spectroscopy and imaging of multiple nuclear species," *Nat. Nanotechnol.* **10**(2), 129–134 (2015).
25. T. Staudacher, F. Shi, S. Pezzagna, J. Meijer, J. Du, C. A. Meriles, F. Reinhard, and J. Wrachtrup, "Nuclear magnetic resonance spectroscopy on a (5-nanometer)³ sample volume," *Science* **339**(6119), 561–563 (2013).
26. H. J. Mamin, M. Kim, M. H. Sherwood, C. T. Rettner, K. Ohno, D. D. Awschalom, and D. Rugar, "Nanoscale nuclear magnetic resonance with a nitrogen-vacancy spin sensor," *Science* **339**(6119), 557–560 (2013).
27. N. Bar-Gill, L. M. Pham, C. Belthangady, D. Le Sage, P. Cappellaro, J. R. Maze, M. D. Lukin, A. Yacoby, and R. Walsworth, "Suppression of spin-bath dynamics for improved coherence of multi-spin-qubit systems," *Nat. Commun.* **3**, 858 (2012).
28. M. Kim, H. J. Mamin, M. H. Sherwood, K. Ohno, D. D. Awschalom, and D. Rugar, "Decoherence of near-surface nitrogen-vacancy centers due to electric field noise," *Phys. Rev. Lett.* **115**(8), 087602 (2015).
29. G. de Lange, Z. H. Wang, D. Ristè, V. V. Dobrovitski, and R. Hanson, "Universal dynamical decoupling of a single solid-state spin from a spin bath," *Science* **330**(6000), 60–63 (2010).
30. L. M. Pham, S. J. DeVience, F. Casola, I. Lovchinsky, A. O. Sushkov, E. Bersin, J. Lee, E. Urbach, P. Cappellaro, H. Park, A. Yacoby, M. Lukin, and R. L. Walsworth, "NMR technique for determining the depth of shallow nitrogen-vacancy centers in diamond," *Phys. Rev. B* **93**(4), 045425 (2016).
31. S. Arroyo-Camejo, A. Lazarev, S. W. Hell, and G. Balasubramanian, "Room temperature high-fidelity holonomic single-qubit gate on a solid-state spin," *Nat. Commun.* **5**, 4870 (2014).
32. V. M. Acosta, E. Bauch, M. P. Ledbetter, A. Waxman, L.-S. Bouchard, and D. Budker, "Temperature dependence of the nitrogen-vacancy magnetic resonance in diamond," *Phys. Rev. Lett.* **104**(7), 070801 (2010).
33. F. Dolde, H. Fedder, M. W. Doherty, T. Nöbauer, F. Rempp, G. Balasubramanian, T. Wolf, F. Reinhard, L. C. L. Hollenberg, F. Jelezko, and J. Wrachtrup, "Electric-field sensing using single diamond spins," *Nat. Phys.* **7**(6), 459–463 (2011).
34. F. Dolde, M. W. Doherty, J. Michl, I. Jakobi, B. Naydenov, S. Pezzagna, J. Meijer, P. Neumann, F. Jelezko, N. B. Manson, and J. Wrachtrup, "Nanoscale detection of a single fundamental charge in ambient conditions using the NV- center in diamond," *Phys. Rev. Lett.* **112**(9), 097603 (2014).
35. M. Fanciulli, C. E. Ascheron, and A. H. Duhm, *Electron Spin Resonance and Related Phenomena in Low-dimensional Structures*, vol. 115 (Springer Berlin Heidelberg, 2009).
36. J. M. Taylor, P. Cappellaro, L. Childress, L. Jiang, D. Budker, P. R. Hemmer, A. Yacoby, R. Walsworth, and M. D. Lukin, "High-sensitivity diamond magnetometer with nanoscale resolution," *Nat. Phys.* **4**(10), 810–816 (2008).

37. L. Robledo, H. Bernien, T. Van der Sar, and R. Hanson, "Spin dynamics in the optical cycle of single nitrogen-vacancy centres in diamond," *New J. Phys.* **13**(2), 025013 (2011).
38. M. S. Grinolds, S. Hong, P. Maletinsky, L. Luan, M. D. Lukin, R. L. Walsworth, and A. Yacoby, "Nanoscale magnetic imaging of a single electron spin under ambient conditions," *Nat. Phys.* **9**(4), 215–219 (2013).
39. M. S. Grinolds, P. Maletinsky, S. Hong, M. D. Lukin, R. L. Walsworth, and A. Yacoby, "Quantum control of proximal spins using nanoscale magnetic resonance imaging," *Nat. Phys.* **7**(9), 687–692 (2011).
40. C. Grezes, B. Julsgaard, Y. Kubo, M. Stern, T. Umeda, J. Isoya, H. Sumiya, H. Abe, S. Onoda, T. Ohshima, V. Jacques, J. Esteve, D. Vion, D. Esteve, K. Mølmer, and P. Bertet, "Multimode storage and retrieval of microwave fields in a spin ensemble," *Phys. Rev. X* **4**(2), 021049 (2014).

1. Introduction

Nitrogen vacancy (NV) color centers, atomic-scale quantum defects embedded in diamond [1], are now the leading modality for nanoscale magnetic sensing, with wide-ranging applications in both the physical and life sciences. For example, single NV center probes have been used for imaging of magnetic vortices [2] and spin waves [3] in condensed matter systems, as well as for single proton magnetic resonance imaging (MRI) [4] and single protein NMR [5]. Ensembles of NV centers have been used for noninvasive sensing of single neuron action potentials [6] and wide-field magnetic imaging of biological cells [7,8] and geoscience samples [9]. Many envisioned applications of NV centers at the nanoscale, such as determining atomic arrangements in single biomolecules [4] or realizing selective strong coupling between individual spins [10] as a pathway to scalable quantum simulations [11], would benefit from a combination of superresolution imaging with high sensitivity magnetometry. NV mapping of magnetic fields with resolution below the diffraction limit has been realized by real-space techniques such as scanned magnetic tips [12] or diamond-AFM probes [13], as well as a Fourier (i.e., *k*-space) method employing pulsed magnetic field gradients [14]. Alternatively, far-field optical superresolution techniques have the advantages of being versatile, simple to integrate into standard NV-diamond microscopes, require no special fabrication, avoid strong magnetic field gradients that can adversely affect the sample to be probed [15], are compatible with a wide range of NV sensing techniques, and allow for fast switching between and selective addressing of multiple NV centers. Coordinate-stochastic superresolution imaging methods, namely STochastic Optical Reconstruction Microscopy (STORM) and Photo Activated Localization Microscopy (PALM), readily offer high parallelization in sparse samples, but are prone to artefacts at high emitter densities and have been implemented until now only for a few NV centers per diffraction limited volume [16,17]. On the other hand, coordinate-deterministic superresolution methods provide targeted probing of individual NV spins with nanometric resolution [18–20], which is well suited for the purpose of coherent nanoscale AC magnetometry, where each NV acts as a local phase-controlled magnetometer probe.

Here, we demonstrate the capability of spin-RESOLFT (REversible Saturable Optical Fluorescence Transitions) as a coordinate-deterministic technique for combined far-field optical imaging and precision magnetometry. In previous work [16] we showed how spin-RESOLFT provides coherent manipulation of NV spins with simultaneous superresolution imaging of NV position. In the present study, we use spin-RESOLFT to map spatially varying magnetic fields at the nanoscale, including the NMR signal from external nuclear spins. Importantly, spin-RESOLFT does not require multi-wavelength excitation and high optical powers, as typically used with STimulated Emission Depletion (STED) [21] microscopy or Ground State Depletion (GSD) by metastable state pumping [22]. As shown below, we use spin-RESOLFT to optically resolve individual NV centers in a bulk diamond sample (Appendix A) with a resolution of about 20 nm in the lateral (*xy*) directions, while exploiting the spin-state dependent optical properties (Fig. 1(a)) and long electronic spin coherence times of NV centers in bulk diamond for precision magnetic field sensing. Moreover, we show that the localization along the beam propagation (*z*) axis can be improved to sub-nanometer precision via combining spin-RESOLFT with NV NMR measurements from proton spins in a sample external to the diamond.

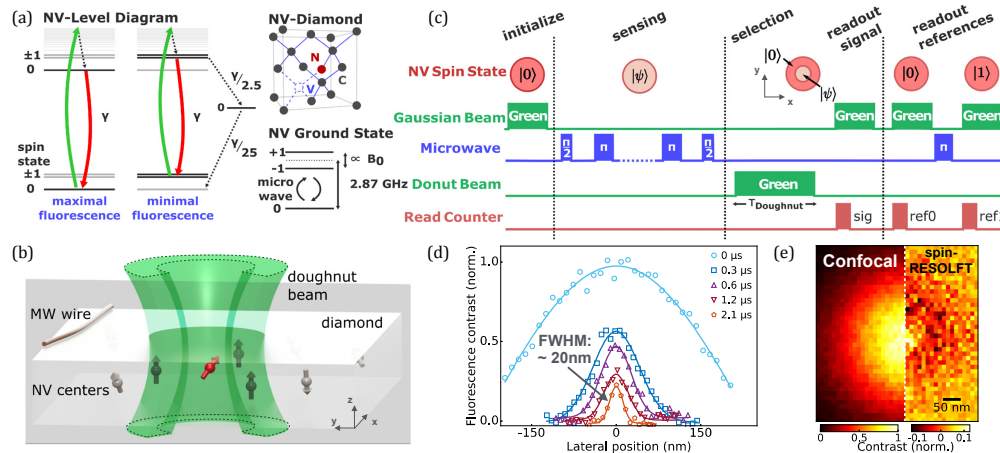


Fig. 1. spin-RESOLFT imaging of NV centers. (a) Energy levels and diamond lattice schematic for the negatively charged NV center in diamond, which has electronic spin $S = 1$. (b) The spin-RESOLFT experimental setup is an NV-diamond scanning confocal microscope augmented with a low power green doughnut beam. (c) Spin-RESOLFT experimental sequence for quantum sensing using NV centers in diamond, e.g., AC magnetometry with the dynamical decoupling pulse sequence shown. A spatially selective repolarisation via the pulsed green doughnut beam is inserted before the spin readout to interrogate only a specific NV center. Readout reference measurements allow calibration of photon count to spin state. (d) 1D spin-RESOLFT scans for a single NV center and different doughnut durations, with doughnut beam power of $700 \mu\text{W}$. (e) 2D spin-RESOLFT image of the same NV as in (d) with similar resolution $\approx 35 \text{ nm}$ but with a much lower doughnut beam power of $25 \mu\text{W}$ and longer duration of $50 \mu\text{s}$. Comparison confocal data in (d) and (e) are normalized to the maximum photon counts. spin-RESOLFT profiles and images are determined by comparing the fluorescence after applying the doughnut (pulse sig) with confocal scans (pulse ref0) and normalized with respect to the maximum spin contrast (see Appendix B).

2. Spin-RESOLFT imaging

Our NV spin-RESOLFT magnetic microscope (Figs. 1(b) and 1(c)) is based on a standard NV-diamond confocal setup. Here, a Gaussian laser beam at 532 nm is used to initialize and readout the NV centers while microwaves at 3 GHz are used to coherently manipulate the NV center ground state electronic spin (Fig. 1(a)). When electronically excited by green light absorption, the $m_s = 0$ spin state largely fluoresces in the red with no change to the spin state, whereas the $m_s = 1$ spin state has a significant probability to decay through a singlet state to the $m_s = 0$ spin state, which effectively reduces the $m_s = 1$ fluorescence rate and allows spin-state initialization into $m_s = 0$. For superresolved NV imaging and spin readout, we overlap a second 532 nm , Laguerre-Gaussian doughnut beam with an intensity zero at the center. Similar to other coordinate-targeted, deterministic superresolution techniques [18, 21, 22], the doughnut beam does not affect NV centers that are located in the dark doughnut center. However, NV centers that are slightly displaced from the dark center, i.e., closer to the doughnut crest, are repolarized by the laser light into the $m_s = 0$ state, and hence all NV spin-state information is erased (see Appendix B).

We first demonstrated how spin-RESOLFT allows imaging of NV centers with subdiffraction resolution given by [18] $FWHM \approx \lambda / [2NA(1 + \Gamma\tau_{\text{doughnut}})^{1/2}]$ in the ideal case. Here, $NA = 1.45$ is the numerical aperture of the objective, Γ is the optical pump rate, and τ_{doughnut} is the duration for which the doughnut beam is applied during the spin-RESOLFT experimental sequence (see Fig. 1(c)). Figure 1(d) shows examples of one-dimensional scans of a single NV center imaged after applying the doughnut beam with power of $700 \mu\text{W}$ and for different durations, with the data fitted numerically using a five level model for the NV

(see Appendix C). For a doughnut duration of $2.1 \mu\text{s}$, we extract a 1D NV image with FWHM $= 20 \pm 2 \text{ nm}$, more than an order-of-magnitude improvement over confocal resolution. We note that the duration of the selective doughnut beam pulse (few microseconds) has minimal effect on the total sequence time (few hundred microseconds). Moreover by adjusting τ_{doughnut} , sub-diffraction NV images can be attained with doughnut powers as low as $25 \mu\text{W}$, ultimately limited by the relaxation time $T_1 \sim 1 \text{ ms}$. Importantly, owing to the long lifetimes of the states harnessed for NV separation, the optical powers required for superresolution are several orders-of-magnitude lower than those required for STED [19, 22]. For example, Fig. 1(e) shows a comparison of two-dimensional images of the same single NV center acquired both without (left) and with (right) the doughnut beam ($25 \mu\text{W}$ power) applied before readout. In practice, the maximum optical resolution is limited by a non-vanishing field intensity at the center of the doughnut mode due to beam shaping imperfections [21], aberrations induced by the sample, as well as thermal and vibrational instabilities of the apparatus (see Appendix D). Reference measurements are interleaved with spin-RESOLFT measurements to allow compensation for slow drifts in the apparatus.

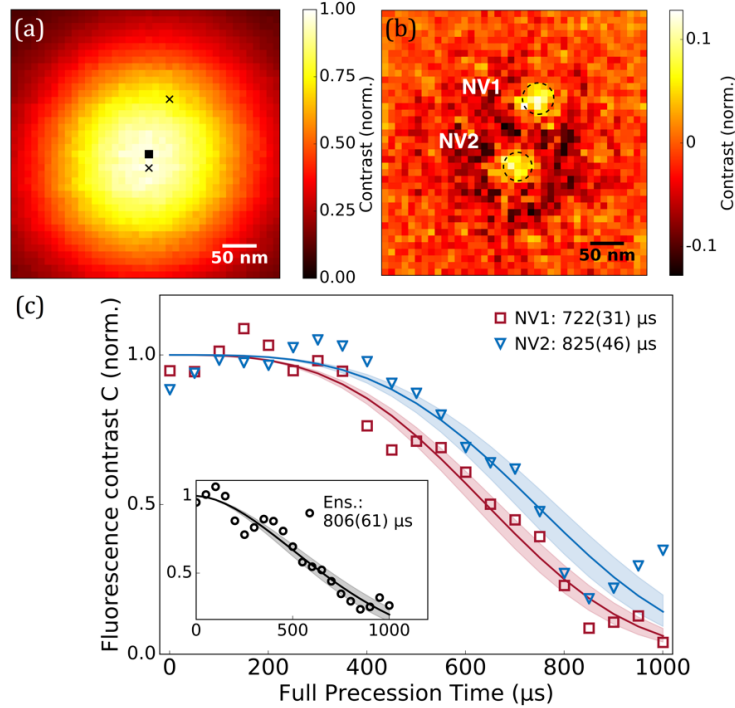


Fig. 2. Spin coherence time measurement for two NV defects resolvable only via spin-RESOLFT. (a) 2D Confocal image of two unresolved NV centres with the same orientation of their spin quantization axes. Black crosses indicate the NV positions as extracted from the spin-RESOLFT image, the black square indicates the Gaussian green laser beam centre. (b) 2D spin-RESOLFT image of same field-of-view as in (a) (acquisition time of 9 s per pixel, $150 \mu\text{W}$ doughnut beam power with duration of $17 \mu\text{s}$). A 50 nm FWHM is extracted using a numerical fit of a five-level model. (c) Selective NV spin coherence measurements and associated fits to a stretched exponential for the two NV centres shown in (a) and (b), using the same doughnut beam power and duration as in (b). Inset: spin coherence time determined for the ensemble of two NVs via a confocal measurement and associated fit. Shaded regions indicate 95% confidence interval extracted from the fits.

3. Superresolution spin manipulation and sensing

3.1 Spin manipulation

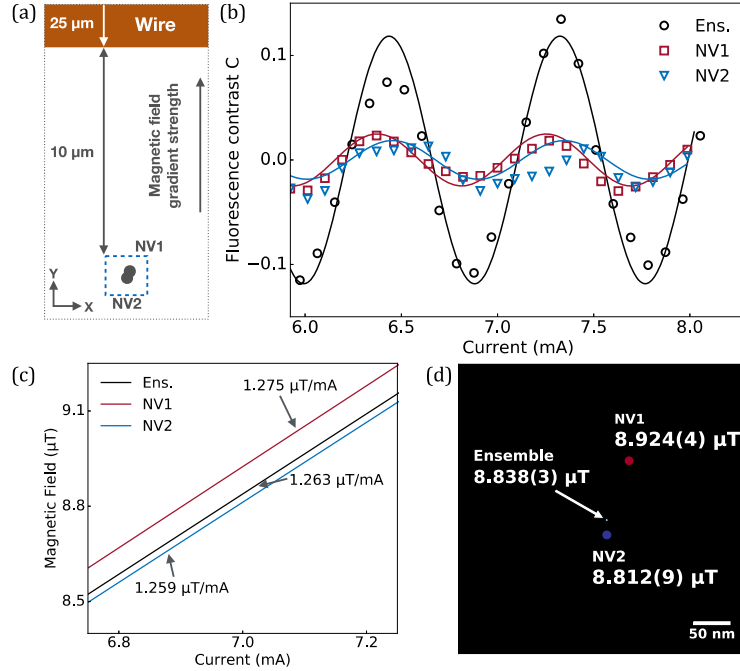


Fig. 3. Superresolution magnetic field imaging for two NV centers via spin-RESOLFT. (a) Schematic of the AC current wire and two NV centers (same as in Fig. 2(b)). (b) spin-RESOLFT AC magnetometry measurements at $V_{AC} = 8.3$ kHz for each NV center individually and for the two NV ensemble in confocal mode. Also shown are fits of data to sinusoids with phase fixed to zero for no applied current. (c) AC magnetic field magnitude at $V_{AC} = 8.3$ kHz as a function of applied current, measured at the position of each NV center via spin-RESOLFT and for the two NV ensemble in confocal mode. (d) 2D magnetic field map created by spin-RESOLFT (at two points) and confocal (one point) measurements at a fixed AC current 7 mA and $V_{AC} = 8.3$ kHz. The size of the disc for each NV is given by the fit uncertainty (95% confidence) of the 2D position from the superresolved NV imaging. For all spin-RESOLFT measurements in this figure, the same doughnut beam power and duration were used as in Fig. 2 (150 μW and 17 μs).

Spin-RESOLFT allows us to manipulate and address individual NV centers within a diffraction limited volume. For example, Fig. 2(a) shows a confocal image of two NV centers that are separated by less than the diffraction limit and can therefore not be resolved by means of confocal microscopy. In comparison, when using spin-RESOLFT microscopy (Fig. 2(b)), the individual NVs are clearly distinguished and their positions are localized within an uncertainty of 5 nm. To demonstrate selective coherent measurements of NV spins using spin-RESOLFT, we begin with measuring the Hahn-echo coherence time (T_2) for each NV individually (Fig. 2(c)) by applying a $\pi/2 - \pi - \pi/2$ MW pulse sequence, followed by spin selective readout using the exact positions for NV₁ and NV₂ extracted from Fig. 2(b) (Appendix E). We find that although the two NVs are subject to a nominally similar spin bath in the diamond sample, the measured T_2 for each NV spin differs due to slight variations in the local environment. The NV ensemble spin coherence time measured in confocal mode is consistent with an average of the two individual NV T_2 values measured with spin-RESOLFT, weighted by the fluorescence collected from each single NV center. Due to a slight systematic mismatch between the doughnut and the Gaussian beam centers, the black

square does not lie exactly in the middle of the crosses indicating the NV positions and therefore the NV ensemble T_2 (inset Fig. 2(c)) is correspondingly closer to the T_2 of NV_2 as measured with spin-RESOLFT.

3.2 Magnetometry

Next, we demonstrated the utility of spin-RESOLFT to deploy each NV within a confocal volume as a very-well-localized, point-like quantum sensor. First, we selectively measured the response of NV_1 and NV_2 to an externally and spatially varying AC applied magnetic field. We also performed ensemble measurements using confocal mode. The field is produced by an AC current that runs through a wire at a 10-micron distance (Fig. 3(a)). The resulting magnetic field gradient, $\Delta B / \Delta r \approx 1$ nT/nm, leads to a measurable difference in field strength for NV_1 and NV_2 . In Fig. 3(b) we plot the measured coherence signal of NV_1 and NV_2 , as well as the ensemble signal, obtained for different magnetic field strengths by incrementally varying the magnitude of the AC current through the wire. The observed oscillations in NV fluorescence contrast are characteristic for spin-based local magnetometry [23]. Note that the contrast in confocal mode is not necessarily the sum of the spin-RESOLFT contrast for NV_1 and NV_2 , as the contrast in spin-RESOLFT depends on the doughnut beam power (Fig. 1(d)). At a fixed current $I_{AC} = 7$ mA (Figs. 3(c) and 3(d)), we measured a magnetic field of 8.924 ± 0.004 μ T for NV_1 and 8.812 ± 0.009 μ T for NV_2 , which is in good agreement with the expected magnetic field profile of the wire (see Appendix F). Doughnut beam imperfections typically reduce the NV spin-state contrast, leading to a trade-off between spatial resolution and magnetic field sensitivity (see Appendix G). As with the NV spin coherence time measurements (Fig. 2), the magnitude of the AC magnetic field found in confocal mode depends systematically on the position of the Gaussian beam and is only a weighted average of the magnetic field magnitudes determined individually for NV_1 and NV_2 using spin-RESOLFT (Fig. 3(d)).

3.3 Spin sensing

To show the applicability of NV spin-RESOLFT for nanoscale magnetic imaging and spectroscopy, we used a shallow NV center located approximately 3 nm below the diamond surface (see below), and simultaneously imaged the NV lateral position with sub-diffraction resolution of 50 nm while sensing the NMR signal from a statistically-polarized nanoscale sample of protons in immersion oil on the diamond surface. Shallow implanted NV centers are a promising modality for quantum computing [11], nanoscale magnetic resonance imaging [24] and single molecule detection [4] due to the strong dipolar and hyperfine interactions with electronic [13] and nuclear [25, 26] spin species located on the diamond surface. Adversely, surface effects tend to shorten the Hahn-echo T_2 of shallow NVs [27, 28], typically to tens of microseconds, which consequently leads to a reduction in magnetic field sensitivity. Thus we integrated spin-RESOLFT with an XY dynamic decoupling protocol to extend [29] the shallow NV T_2 and enable practical nanoscale NMR imaging (Fig. 4(a)). The dynamic decoupling protocol creates a coherent superposition of the NV $m_s = 0$ and $m_s = 1$ spin states, and then alternates this spin coherence between free evolution (of duration τ) and π phase flips, before converting the total accumulated phase into an NV spin state population that is measured optically (Fig. 4(b)). We find that spin-RESOLFT can be combined with dynamical decoupling sequences to increase the NV coherence time to at least 100 μ s while providing superresolution. Moreover, the NV spin phase accumulation is strongly perturbed when a frequency component of the external magnetic field matches twice the free evolution period $\tau = \nu_B / 2$. Thus we observed a spectrally narrow dip in the NV coherence signal (Fig. 4(c)) at the proton spin Larmor precession frequency $\nu_p = (\gamma_p / 2\pi) B_0 \approx 1.2$ MHz, which is indicative of an NMR signal from statistically-polarized proton spins in the immersion oil on the diamond surface [25]. Here, γ_p is the proton spin gyromagnetic ratio and $B_0 = 28.2$ mT

is the applied static magnetic field. Importantly, we find that the spin-RESOLFT and confocal mode NMR measurements are consistent: e.g., application of a 10 μ s long doughnut beam pulse of 30 μ W average power does not deteriorate the proton NMR signal, while allowing for far-field optical spin readout of a sub-diffraction sized area with a lateral diameter of around 50 ± 5 nm. Furthermore, by fitting the NV NMR data to an analytical model (see Appendix H), we determined the depth of the NV quantum sensor below the diamond surface to be 3.0 ± 0.3 nm [30].

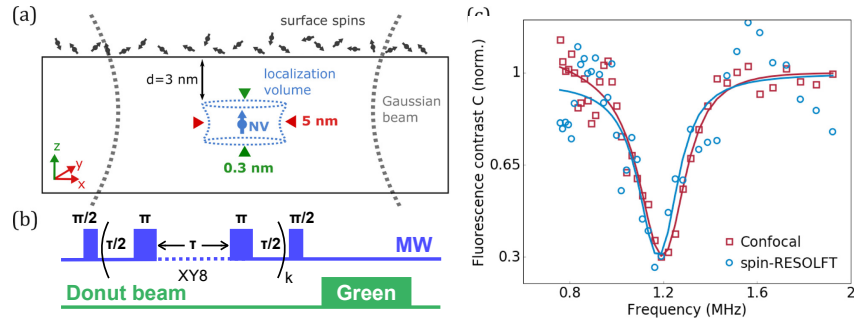


Fig. 4. NV spin-RESOLFT sensing of proton NMR. (a) Schematic showing nanometer-scale localization volume of a shallow NV. (b) XY8-k dynamical decoupling pulse sequence used for NMR proton sensing with sub-diffraction resolution. (c) Example use of an XY8-4 sequence for spin-RESOLFT (blue) and confocal (red) NV NMR spectroscopy of proton spins in immersion oil on the diamond surface without degradation of the measured NMR proton linewidth (with doughnut beam power of 30 μ W and duration of 10 μ s). Fits to an analytical model (red and blue curves) determine the NV depth to be 3.0 ± 0.3 nm [30].

4. Conclusion

In conclusion, we used spin-RESOLFT to selectively image and coherently manipulate two NV centers within a confocal volume, with no corrupting effect on NV spin coherence, enabling sensitive nanoscale magnetic imaging and spectroscopy. By combining this technique with spin sensing via dynamical decoupling sequences applied to shallow NVs, we demonstrated the utility of spin-RESOLFT for nano-NMR. In comparison to other NV-diamond approaches for nanoscale magnetic imaging, such as scanning probe [11, 12] and Fourier techniques using strong pulsed field gradients [10], spin-RESOLFT is technically straightforward, as it is all-optical and can be realized via extension of a confocal microscope (Appendix I). In future work we will extend spin-RESOLFT to many NVs within a diffraction-limited spot, allowing a diverse range of nanoscale magnetic imaging applications in both the physical and life sciences. We also anticipate that spin-RESOLFT will enable precise determination of the distance between two NV qubits, as well as their coherent manipulation. For a separation of 20 nm, the spin-spin vectorial interaction between individual NV centers (~ 10 kHz) is larger than their typical decoherence rate (~ 1 kHz), fulfilling a fundamental requirement for many quantum information protocols [10, 31]. Furthermore, low-power superresolution imaging techniques such as spin-RESOLFT can be critical for many applications, e.g., those that require cryogenic temperatures or shallow NV centers or for light-sensitive biological samples, as high optical power can cause heating as well as surface and sample deterioration. Finally, we expect that spin-RESOLFT can be straightforwardly extended to other NV-based sensing modalities, including temperature [32], electric field [33], and charge state [34] detection with nanoscale optical resolution.

Appendix A. Diamond sample information

Sample A used in Figs. 1(d), 1(e), 2, and 3 of the main text is an ultra-pure CVD diamond, isotopically engineered (99.99% ^{12}C) with NV density of $\sim 3 \times 10^{12} \text{ cm}^{-3}$, NV orientation along two of four crystal axes, NV spin coherence time (T_2) approaching one millisecond, and NV

spin lattice relaxation time T_1 of a few milliseconds. Sample B used for measurements shown in Fig. 4 is also an ultra-pure CVD sample, isotopically engineered (99.999% ^{12}C) with shallow implanted NV centers 1 - 20 nm below the surface (^{14}N at 2.5 keV) at a density of $1.4 \times 10^{12} \text{ cm}^{-2}$, NV orientation along all four crystal axes, and NV $T_2 \sim 30 \mu\text{s}$. All measurements were made at room temperature. Both samples were created by Element Six.

Appendix B. Spin-RESOLFT technique

By first applying a π -pulse to switch all the NV centers into the spin state $m_s=1$ and then using a selectively repolarizing green doughnut beam, we pump off-center NVs into the $m_s=0$ ground-state. These off-center NV centers contribute a spatially broad ‘background’ fluorescence signal in addition to a spatially narrower fluorescence feature characteristic of superresolved NV centers in the center of the doughnut beam (green curve in Fig. 5(a)). We determine the background from the off-center NVs by recording a confocal scan (blue curve in Fig. 5(a)) immediately following the scan acquired with the doughnut beam. By subtracting the two signals, we obtain the 1D spin-RESOLFT image, which displays a non-Gaussian intensity profile (Fig. 5(b)). In Figs. 1(d) and 1(e) and Figs. 2(a) and 2(b), the intensity profiles are normalized with different normalization procedures to allow for a straightforward graphical comparison. Confocal intensity profiles are normalized by the maximum photon counts: $I = \text{sig}(x)/\text{sig}(0)$. Spin-RESOLFT profiles are normalized by the maximum spin contrast ($\text{ref0} - \text{ref1}$): $C = (\text{sig}(x) - \text{ref0}(x)) / (\text{ref0}(0) - \text{ref1}(0))$. The observed profile is strongly dependent on the degree of NV spin repolarization that occurs when the doughnut beam is applied, which is discussed below. We note that the intensity profiles in Fig. 1(d) were taken under conditions of short doughnut pulse duration, permitting us to approximate the linewidth as Gaussian.

Spin-RESOLFT provides fast switching between emitters because it is a deterministic superresolution imaging technique, in contrast to STORM/PALM techniques that rely on the stochastic fluorescence behavior of emitters at low illumination powers. Thus, spin-RESOLFT allows one to arbitrarily and quickly choose an NV sensor of choice and acquire information about the magnetic field at a particular local position. Moreover, the dead time induced by the presence of the doughnut beam is negligible, as the doughnut pulse is shorter than typical sensing times. In the case of spin-RESOLFT magnetic imaging, the data acquisition time is determined by the finite fluorescence rate of NV centers as well as the scanning parameters used to obtain high-resolution images.

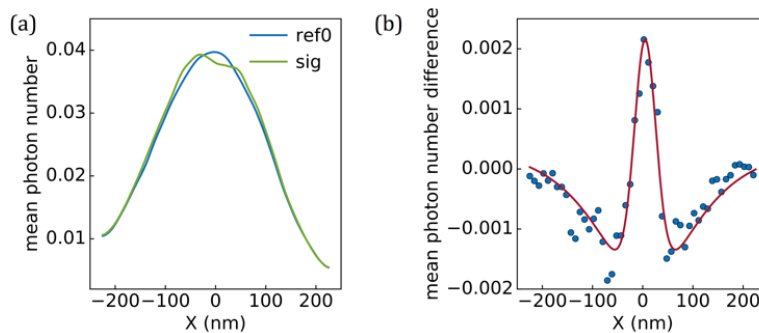


Fig. 5. (a) Single NV fluorescence measurements as a function of relative position (1D) acquired for the spin-RESOLFT protocol: after the application of the doughnut beam (signal, green) and after a complete repolarization with a Gaussian beam (ref0, blue). A 2-pixel running average is applied to smooth shot-noise-limited intensity fluctuations. At certain positions, the NV spin repolarization occurring from doughnut beam illumination is more efficient, leading eventually to a stronger fluorescence signal. (b) 1D spin-RESOLFT NV image (blue dots) constructed by subtracting the fluorescence curves shown in (a). Red curve is a numerical fit of data to a five level model (see next section).

In Fig. 2(b) of the main text, we show that two NV centers within the same diffraction-limited volume are distinguished by the spin-RESOLFT technique. From the correlated spin-RESOLFT image we extract the distance between the two NV centers to be $d = 105 \pm 16$ nm. Due to a ≈ 20 nm misalignment between the Gaussian readout and doughnut beams, the maximum fluorescence in the confocal image is not perfectly aligned with the axis formed by the two NV centers.

Appendix C. NV spin repolarization

Due to the spin-dependent intersystem crossing through its singlet states, NV centers preferentially decay into the $m_s=0$ ground state under green illumination. This results in strong spin polarization after several excitation cycles. In spin-RESOLFT, the role of spin polarization is two-fold: preparing the initial NV state in $m_s=0$ for sensing using a Gaussian beam, and repolarizing the NV center into $m_s=0$ for superresolution imaging using the doughnut beam. As mentioned in the main text and shown in the inset of Figs. 2 and 5, the fluorescence point-spread function (PSF) displays a non-trivial shape that is the result of non-linear NV repolarization. To model the NV polarization dynamics, we use the five-level system shown in Fig. 6.

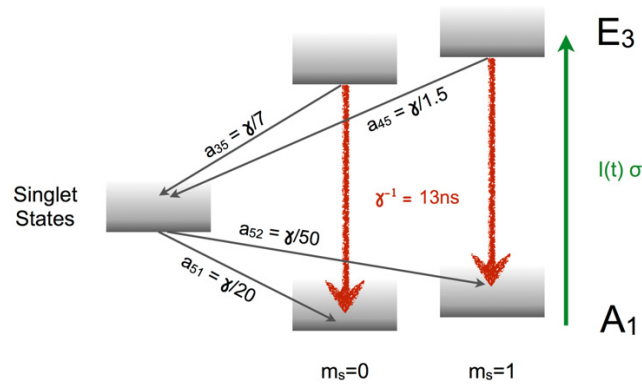


Fig. 6. NV level structure and decay rates. The populations are denoted by n_i , where i refers to the following levels: 1 for $m_s = 0$ ground state, 2 for $m_s = -1$ ground state, 3 for $m_s = 0$ excited state, 4 for $m_s = -1$ excited state and 5 for the singlet states. The decay rates a_{ij} between levels are indexed by the initial level i and the final level j . All rates are given relative to the primary fluorescence decay rate γ . The singlet states are represented as a single state for the sake of simplicity, and we use previously measured room temperature rates [37].

The system of rate equations that governs the NV state populations under optical excitation can be formulated as

$$\frac{1}{\gamma} \frac{dn_1}{dt} = -I(t) \sigma \cdot n_1 + n_1 + a_{51}n_5 \quad (1)$$

$$\frac{1}{\gamma} \frac{dn_2}{dt} = -I(t) \sigma \cdot n_2 + n_2 + a_{52}n_5 \quad (2)$$

$$\frac{1}{\gamma} \frac{dn_3}{dt} = I(t) \sigma \cdot n_1 - n_3 - a_{35}n_3 \quad (3)$$

$$\frac{1}{\gamma} \frac{dn_4}{dt} = I(t) \sigma \cdot n_2 - n_4 - a_{45}n_4 \quad (4)$$

$$\frac{1}{\gamma} \frac{dn_5}{dt} = a_{35}n_3 + a_{45}n_4 - a_{51}n_5 - a_{52}n_5. \quad (5)$$

Here σ represents the cross-section of the primary NV electronic transition for a 532 nm laser beam pulse of intensity $I(t)$. Figure 7 shows the $m_s = 0$ ground state population after applying a square pulse starting at $t = 0$ on an unpolarized NV center with equal initial spin state population. We see that the degree of repolarization depends on both the intensity and duration of the excitation pulse. In particular, a higher degree of polarization is achieved with a long and weak green pulse (5 ms at 5% of the saturation intensity). Moreover, for a fixed pulse duration, we find that the repolarization is non-linear in optical intensity, resulting in a strong effect on the PSF of the spin-RESOLFT microscope image determined by the spatial intensity distribution of the doughnut beam.

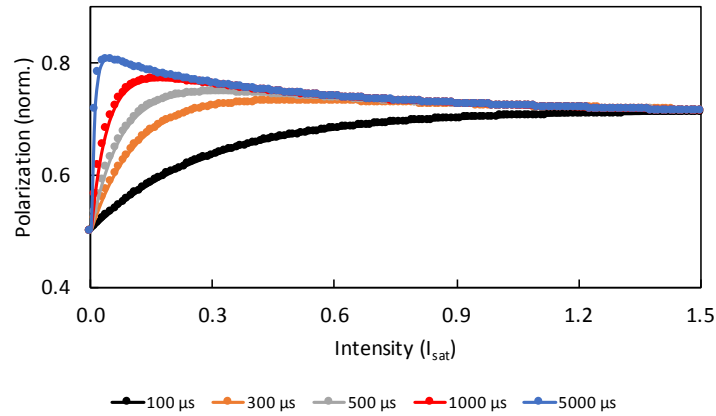


Fig. 7. Simulation of the dependence of the NV spin polarization on green excitation beam intensity. The degree of polarization displays a non-linear behaviour with light excitation. Short pulses of about 100 μ s provide at most 70% polarization, due to non-zero decay rates from the singlet state to both the ground state sublevels. Longer pulses provide a higher degree of polarization but restrict the intensity to a fraction of the saturation intensity. The highest resolution is obtained for durations where the slope near the doughnut center is steeper, which leads to strong non-linear behaviour, a degradation of the spin polarization far from the doughnut center and a non-trivial PSF profile.

Indeed, the doughnut intensity profile can be approximated near the center as

$$I(r) = I_0 \left(\left(\frac{r}{r_0} \right)^2 + \epsilon \right) \exp \left(- \left(\frac{r}{r_0} \right)^2 \right) \quad (6)$$

where I_0 is the peak intensity, r_0 is the doughnut radius, and ϵ is the relative residual intensity in the doughnut center. Using this intensity profile as input to the system of Eq. (1)–(5), we plot the one-dimensional spin-RESOLFT PSF in Fig. 8 for two different values of $\epsilon = 0.1\%$ and $\epsilon = 2\%$. As the intensity increases quadratically along the doughnut profile, the degree of NV polarization is convolved with the behaviour displayed in Fig. 7. Higher resolution is achieved for combinations of long durations and weak powers, which display strong repolarization. However, for a particular finite position in the doughnut profile, the intensity reaches the value where the repolarization is maximum before decreasing back to the steady value of 70%, which leads to negative contrast and non-Gaussian wings in the spin-RESOLFT PSF. Negative contrast should be understood as a polarization that is greater than the reference case of repolarization with a long or strong pulse. Doughnut imperfections, which lead to a non-zero intensity ϵI_0 in the doughnut beam center, tend to reduce the state

dependent fluorescence contrast, but do not affect the shape of the intensity profile. We use the numerical solution to Eq. (1)–(5) to extract the resolutions reported in Figs. 1(d), 1(e), and 2(b) in the main text.

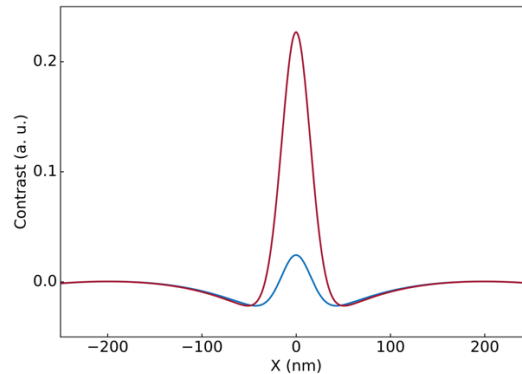


Fig. 8. Simulated spin-RESOLFT PSF for two different residual intensities in the center of the green doughnut beam: $\epsilon = 0.1\%$ (red) and $\epsilon = 2\%$ (blue).

Appendix D. NV position drift and fluctuations

Because of separated optical paths, the spin-RESOLFT experimental setup is sensitive to the relative motion of the Gaussian beam, doughnut beam, and confocal PSF, over the typical timescale of a complete experiment (minutes to hours). In particular, a single realization of a spin-RESOLFT experimental sequence requires $\sim 20 \mu\text{s}$, yielding ~ 0.02 collected photons. The sequence is repeated $\sim 20,000$ times for each imaging pixel to suppress photon shot noise to 5%. Thus, a full 1D scan of $\sim 400 \text{ nm}$ (100 pixels) across an NV center ideally takes $\sim 40 \text{ s}$. However, due to overhead from data recording and display, such a single 1D scan actually requires $\sim 2 \text{ min}$. In addition, between each scan the position of the NV center is recorded, and then the optical illumination is adjusted to place the NV back into the middle of the scan window. The tracking procedure consists of discrete probing of the fluorescence spatial distribution in the neighborhood of the NV center to determine the position of its maximum value. It is followed by 1D confocal scans in both lateral directions that are fitted with Gaussians to obtain the NV center position with a precision of about 5 nm. For the single NV spin-RESOLFT datasets plotted in Fig. 1(d) of the main text, the entire 1D scan is repeated and then averaged 6 times, leading to a total acquisition time of about 12 min. In the case of multiple NV imaging (Figs. 2 and 3 of main text), the tracking is done by taking a single nearby NV as reference. The reference NV is positioned about $1 \mu\text{m}$ away from the pair of NV centers, as shown in Fig. 9. In the more general case of a wide field-of-view image, optical reflection from a golden nanoparticle attached on the surface of the diamond is used as a reference point.

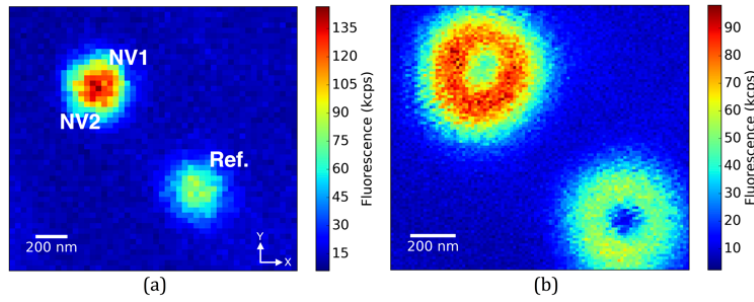


Fig. 9. Measured 2D images of a pair of proximal NV centers and a reference NV center (a) confocal scan; (b) green doughnut beam scan.

During long acquisition times, the position of an NV center shows a strong correlation with laboratory temperature fluctuations, as shown in Fig. 10. Due to thermal expansion of the objective holder, we observed drifts of the reference NV by approximately 500 nm. These drifts were minimized by using insulating enclosures in which the temperature fluctuates by not more than 0.1 °C over the course of a measurement. Nonetheless, such diminished drifts as well as table vibrations during a line scan can still result in observable broadening of the PSF of the spin-RESOLFT microscope. 2D scans, which are usually acquired over 10 hours, are affected even more severely. Figure 10(b) displays the relative displacement of the NV center used in Fig. 1(d) of the main text after each line scan. From this trace, we identify a motion along the direction of the scan with a standard deviation of 11 nm.

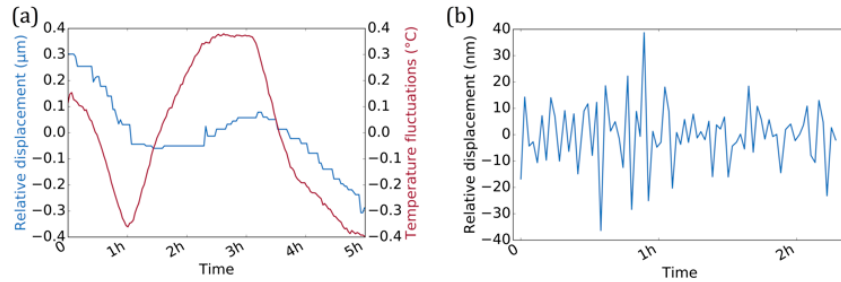


Fig. 10. (a) Measured relative 1D position of an example NV center and the laboratory temperature during a 5h-long confocal scan. A 1D NV fluorescence intensity profile takes about 1 minute after which the temperature and the NV center position are recorded. The laboratory temperature oscillates with a period of about 1 h and induces a correlated drift of the NV center position ~500 nm. (b) Stabilization of the laboratory temperature to a peak-to-peak variation of 0.1 °C allows data acquisition for two hours during which time the NV position is stable with a standard deviation of 11 nm.

Appendix E. NV spin coherence measurements

There is a rapid dephasing of freely precessing NV spins on a time scale $T_2^* \sim 0.1\text{--}10\ \mu\text{s}$ for typical spin impurity concentrations in diamond. By applying a single resonant MW pulse to refocus the dephasing, the Hahn-echo sequence decouples NV spins from spin bath magnetic field fluctuations that are slow compared to the free precession time. In diamond Sample A used in Fig. 2 and Fig. 3, the low impurity concentration leads to a long NV Hahn-echo spin coherence time T_2 of about 800 μs . Such coherence times are extracted from fits of Hahn-echo measurements of NV spin coherence to a stretched exponential coherence function

$$C(t) = A \exp\left(-\frac{t}{T_2}\right)^p, \text{ where the parameter } p \text{ is related to the spin bath surrounding the NV}$$

center [35]. For spin-RESOLFT measurements of individual NVs, $p_{\text{NV1}} = 3.2 \pm 0.3$ and

$p_{\text{NV}_2} = 3.5 \pm 0.5$ are found, which are in good agreement with the expected value $p = 3$ for a spin bath with Lorentzian spectral density [27, 35]. In confocal mode, the incoherent dynamics of these two NV centers results in a reduced value for $p = 1.7 \pm 0.2$ as expected.

Appendix F. AC magnetic field gradient

To create an AC magnetic field gradient, which results in a measurable difference in magnetic field strength at the position of NV_1 and NV_2 as used for the results in Fig. 3 of the main text, we drive an AC current $I_{\text{AC}} = 7$ mA at 8.3 kHz through a copper wire (type Alfa Aesar, diameter 25 μm) that is ~ 10 μm from the NVs. The same wire also carries the microwaves for coherent NV spin manipulation.

To simulate the observed magnetic field dependence, we devised a simple model that takes the projection of the applied AC fields onto the NV axis into account. In our geometry, the wire is parallel to the horizontal axis of Figs. 2(b) and 3(d) (here, the y-direction), whereas the z-direction corresponds to the normal of the diamond's top surface and the x-direction completes the orthonormal reference frame. The NV center axis is determined by its polar θ and azimuthal ϕ angles, as commonly defined. In this system of coordinates, NV_1 and NV_2 are directed along the x-direction ($\phi = 0^\circ$) while making an angle with the z-axis of $\theta = 54.7^\circ$. Moreover, the magnetic field lines form loops in the plane perpendicular to the wire. In AC magnetometry, the NV center is sensitive to the component of the magnetic field that is parallel to the NV axis, namely

$$\begin{aligned} B_{\parallel}(\vec{r}) &= B_{\text{wire}}(\vec{r}) \cdot \text{NV}(\vec{r}) \\ &= \frac{\mu_0}{2\pi} \frac{I}{x^2 + z^2} (z \sin \phi \cos \theta + x \cos \phi). \end{aligned} \quad (7)$$

In Fig. 11(a), we simulate this magnetic field component for different positions along the x direction, with the center of the wire fixed at the origin and the NV center's depth is chosen to be at $z = 12.5 + 7.5$ $\mu\text{m} = 20$ μm under the wire. When the NV center is at $x = -10$ μm from the wire's edge, we find the calculated field along the NV center axis to be 9 μT , which is in good agreement with the experimental values we measure and report in the main text. Moreover, we plot the magnetic field gradient expected from this model as function of the x position in Fig. 11(b). The value of the magnetic field gradient of about 1 nT/nm is also in good agreement with the gradient experimentally measured with the pair of NV centers (NV_1 and NV_2) separated by 105 nm.

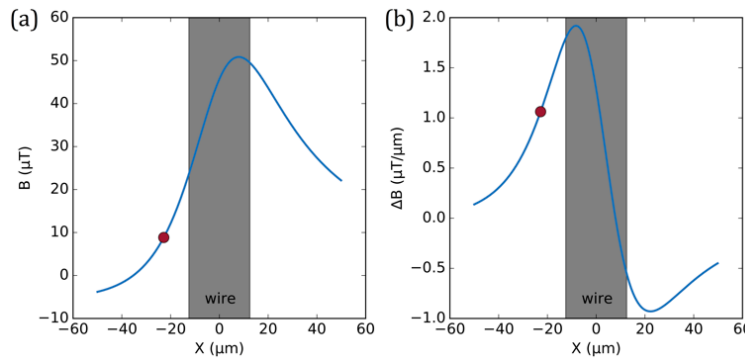


Fig. 11. (a) Magnetic field strength and (b) gradient extracted from a model that takes into account the distance from the wire and the orientation of the NV center axis. At a horizontal distance of 10 μm from the wire, the measured magnetic field strength of 9 μT and (b) measured gradient of 1 nT/nm are in good agreement with the experimental values reported in the main text.

The NV Rabi frequency's spatial dependence can also be derived from this model by considering the MW field component perpendicular to the NV axis, which is

$$B_{\perp}(\vec{r}) = B_{\text{wire}}(\vec{r}) - B_{\text{wire}}(\vec{r}) \cdot NV(\vec{r}). \quad (8)$$

Using the same experimental conditions as described above, we calculate a Rabi frequency of 5.5 MHz for a current of 30 mA. This is also in a good agreement with the measured Rabi frequency for this MW current in our setup (Fig. 12).

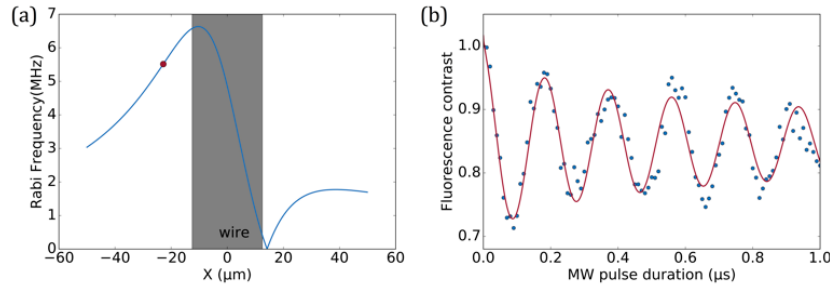


Fig. 12. (a) Calculated NV Rabi frequency as a function of the NV center horizontal position. This spatial behaviour is calculated from a model that takes into account the distance between the wire and the NV center as well as the NV orientation. The red dot corresponds to the position of the two NV centers used in the main text (NV1 and NV2). (b) Measured NV Rabi oscillations (blue dots) and a fit to an exponentially damped sinusoid (red curve). The extracted Rabi frequency of 5.5 MHz is in a good agreement with the model calculation.

Appendix G. NV magnetometry

The magnetic field sensitivity in a Hahn-Echo pulse sequence has the following expression [36]:

$$\eta = \frac{1}{\gamma_e} \frac{1}{C e^{-\tau/T_2}} \frac{\sqrt{t_i + \tau + t_R}}{\tau} \quad (9)$$

where γ_e is the electron gyromagnetic ratio, C is the maximum spin contrast achievable in spin-RESOLFT imaging at a specified resolution, t_i, t_R are the initialization and readout time.

Because of experimental imperfections such as non-zero intensity at the doughnut center, the NV spin-state contrast decreases as we apply longer a doughnut laser beam to reach sub-diffraction resolution, which results in a degradation of the magnetic field sensitivity. For example, in the case of Fig. 3(b), we obtain a sensitivity of $\sim 60 \text{ nT}/\sqrt{\text{Hz}}$ in confocal mode with a single NV, and $\sim 250 \text{ nT}/\sqrt{\text{Hz}}$ with spin-RESOLFT for 50 nm spatial resolution as the contrast drops by a factor of about 4 from $\sim 10\%$ to $\sim 2.5\%$.

Appendix H. Proton NMR measurements

XY8-k pulse sequences are applied to a single shallow NV to measure the NMR signal produced by ~ 100 statistically-polarized protons spins in immersion oil placed on the diamond surface. These pulse sequences produce NV spin phase accumulation that is transferred to a spin state population difference by means of the last microwave $\pi/2$ pulse. The choice of the phase of this last pulse allows for projections onto each NV spin state $m_s=0$ and $m_s=1$, resulting in fluorescence measurements F_0 and F_1 . Common-mode noise from laser fluctuations is suppressed by normalizing the fluorescence signals together in a fluorescence contrast $C = (F_0 - F_1) / (F_0 + F_1)$. NV sensing of the magnetic field Fourier components at frequencies ν is realized by measuring the fluorescence contrast C over a range of free

evolution times $\tau = \nu/2$. NV spin “background” decoherence is characterized by slow exponential decay of the fluorescence signal over hundreds of microseconds (Fig. 2(c) of the main text). This background decoherence is fit to a stretched exponential function and normalized out, leaving only the narrower proton-NMR-induced dip in NV signal contrast on top of a flat baseline, as shown in Fig. 4(b). The shape of this dip is determined by the magnetic field fluctuations produced by the dense ensemble of proton spins in the immersion oil on the diamond surface, as well as by the filter function corresponding to the XY8-k dynamical decoupling pulse sequence. The magnetic field signal has cubic dependence on the distance between the NV center and diamond surface ($B_{\text{RMS}} \propto d_{\text{NV}}^{-3}$), which can be then

estimated by fitting the dip with the following formula: $C(\tau) \approx \exp\left(-\frac{2}{\pi^2} \gamma_e^2 B_{\text{RMS}}^2 K(N\tau)\right)$.

Here B_{RMS} is the RMS magnetic field signal produced at the Larmor frequency by the proton spins, $K(N\tau)$ is a functional that depends on the pulse sequence and the nuclear spin coherence time, and N is the number of pulses, which are separated by the NV spin free precession time τ . A thorough derivation of this formula as well as the description of the functional $K(N\tau)$ is presented by Pham et al. [30].

Appendix I. Technique comparison

Table 1. Technique comparison.

	spin-RESOLFT	Diamond-AFM [38,39]	Fourier imaging [14]
Apparatus	Doughnut beam, Scanning stage	AFM, Scanning stage	Micrometer-coil
Imaging speed	9 sec/pixel	7 sec/pixel	3.42 sec/pixel
Resolution	20 nm (1D/2D)	8.9 nm (1D/2D)	2.6 nm (1D) 30 nm (2D)
AC Sensitivity	60-250 nT/Hz ^{1/2}	56 nT/Hz ^{1/2}	1200 nT/Hz ^{1/2}
Application	Life science Low temperature, Spin and molecule detection	Condensed matter physics	Quantum information science, Condensed matter physics

The three nanoscale NV magnetic imaging techniques mentioned in the main text have very different features, which we summarize in Table 1. First, we note that all three techniques provide similar imaging resolution and speed. The diamond-AFM technique [38, 39] offers high sensitivity that is not affected by background fluorescence caused by off-axis NV centers. The resolution is tunable by adjusting the DC gradient, but is limited by the distance between the target and the single NV center located in the AFM tip. In addition, the method is technically challenging, requiring difficult nanofabrication and exquisite vibrational isolation, which makes it difficult to use this technique for samples with rough surfaces or for single molecules. It is expected to best suited for the study of magnetic

materials. The Fourier magnetic imaging technique [14] provides outstanding resolution and speed, but with degraded sensitivity, technical complexity, and nontrivial heating. Specifically, the technique uses micrometer-sized coils, fabricated on a support in contact with the diamond, to generate strong pulsed magnetic field gradients, with resolution $\Delta r \propto 1/B_{grad}$. The associated strong pulsed electrical currents can induce significant sample heating and therefore require well-engineered thermal isolation and cooling. These strong magnetic fields gradients can also adversely affect some classes of samples. Finally, spin-RESOLFT provides a reasonable combination of spatial resolution, sensitivity, and imaging speed, as well as other complementary features: (i) it is all-optical; (ii) it can be realized via straightforward extension of a confocal microscope; and (iii) it is suitable for low temperature experiments where laser powers of ~ 1 mW laser are already a strong constraint and can raise the temperature by few hundreds of millikelvins [40].

Funding

U. S. Army Research Laboratory and the U. S. Army Research Office (grant number W911NF1510548); Defense Advanced Research Projects Agency (DARPA) (QuASAR program, grant number HR0011-11-C-0073); National Science Foundation (NSF) (award EPMD-1408075); the National Security Science and Engineering Faculty Fellowship program; and the Gordon and Betty Moore Foundation.

Acknowledgments

It is a pleasure to thank K. Arai, N. Bar-Gill, D. Glenn, P. Maurer, M. Ku and H. Zhang for stimulating discussions.